



OPEN ACCESS

EDITED BY

Jesus Manuel Munoz-Pacheco,
Benemérita Universidad Autónoma de Puebla,
Mexico

REVIEWED BY

Gurpreet Kaur,
Amity University, India
Daniel Clemente-Lopez,
National Institute of Astrophysics, Optics and
Electronics (INAOE), Mexico

*CORRESPONDENCE

Ping-Ping Zeng,
✉ ppzeng@ncu.edu.cn

RECEIVED 10 October 2023

ACCEPTED 22 December 2023

PUBLISHED 02 February 2024

CITATION

Zeng P-P, Zhou X, Zhong D-F, Chen S-H and
Gong L-H (2024), Color watermarking
algorithm combining the quantum discrete
cosine transform with the sinusoidal–tent map.
Front. Phys. 11:1315765.
doi: 10.3389/fphy.2023.1315765

COPYRIGHT

© 2024 Zeng, Zhou, Zhong, Chen and Gong.
This is an open-access article distributed under
the terms of the [Creative Commons Attribution
License \(CC BY\)](#). The use, distribution or
reproduction in other forums is permitted,
provided the original author(s) and the
copyright owner(s) are credited and that the
original publication in this journal is cited, in
accordance with accepted academic practice.
No use, distribution or reproduction is
permitted which does not comply with these
terms.

Color watermarking algorithm combining the quantum discrete cosine transform with the sinusoidal–tent map

Ping-Ping Zeng^{1*}, Xi Zhou², De-Fei Zhong², Su-Hua Chen² and Li-Hua Gong³

¹College of Science and Technology, Nanchang University, Jiujiang, China, ²Department of Electronic Information Engineering, Nanchang University, Nanchang, China, ³School of Electronic and Electrical Engineering, Shanghai University of Engineering Science, Shanghai, China

To overcome the drawbacks of the existing sinusoidal map and tent map, this paper proposes the design of a sinusoidal–tent (ST) map. The test results indicate that the new chaotic system exhibits more significant advantages in chaos control. Compared with the sinusoidal map and tent map, the proposed sinusoidal–tent map performs better in terms of bifurcation diagram and Lyapunov exponents. The trajectories of the sinusoidal–tent map can occupy all the phase planes over (0,4), while those of the two classic maps only occupy a small phase space, and the Lyapunov exponents of the ST map are all positive within the range of control parameters, higher than those of seed maps. Simultaneously, a novel quantum scrambling operation is devised based on the sinusoidal–tent map to avoid the periodicity of the quantum Arnold scrambling method. Initially, two chaotic sequences are generated to scramble the pixel positions of the watermark image, further enhancing the security of the watermarking algorithm. Subsequently, the host image is processed by the quantum discrete cosine transform, and finally, the scrambled watermark image is inserted into the medium-frequency band of the transformed host image, ensuring the invisibility of the watermarking. According to the simulation results, the quantum watermarking algorithm has excellent invisibility and robustness.

KEYWORDS

quantum watermarking, quantum discrete cosine transform, sinusoidal–tent map, quantum color image representation, image copyright

1 Introduction

Information security is indeed a crucial field in the era of big data. Image information security is one of its significant branches that have witnessed rapid development over the past few decades [1–5]. Particularly, benefiting from the entanglement characteristics and the powerful parallel computing abilities, quantum computing has the potential to overcome the limitations of classical computation. Quantum computing is a computational model that employs quantum bits, utilizing the principles of quantum mechanics to process information. Traditional computers use bits (0 or 1) as the smallest units for storage and processing, while quantum computers use quantum bits, often referred to as “qubits.” Qubits can not only represent the states of 0 and 1 but also exist in superpositions of these states, a key aspect of quantum parallelism [6].

During signal transmission, the computing complexity of quantum operations has been effectively reduced, thereby significantly increasing information security through quantum computing. Beach et al. [7] highlighted and analyzed the doubts surrounding quantum image processing, demonstrating the true quantum superiority in quantum image classification and recognition. To improve the fault tolerance of quantum circuits, Li et al. [8] implemented cyclic and complete translations on quantum images through quantum arithmetic operations and realized the scalar matrix multiplication by designing fault-tolerant circuits for these operations with the TR and Peres gates. The mid-point filter, which is an order statistic filter, cannot be directly used in the frequency domain. As a solution, Ali et al. [9] introduced a new quantum mid-point filter designed specifically for spatial domain applications. This proposed approach maintains the same level of noise suppression as the classical version but significantly reduces the complexity.

For different purposes, various representation models of quantum images have been investigated [10–14]. The first flexible representation of the quantum image (FRQI) was invented to encode the position information and color information of an image into a single quantum state [10]. A novel enhanced quantum representation (NEQR) was explored to quadratically speed up the preparation of quantum images and enhance the compression ratio of quantum images [11]. The radiation energy value of a pixel in infrared images could be stored using the probability of projection measurement [12]. A quantum scaling-up algorithm for images was proposed using nearest-neighbor interpolation [14]. In addition, researchers have also developed several models for quantum color image representation, such as NCQI [15], MQIR [16], and DQRCI [17].

Digital watermarking is a technique that embeds specific information within digital media, with the aim of verifying or identifying the authenticity, ownership, or source of digital content. This technology is commonly used in digital media files such as images, audio, and videos [18]. To address the security issue in copyright protection, various watermarking strategies have been explored [19, 20]. Gong et al. [19] proposed a watermarking scheme for double-color images, which involved the use of quaternion fractional-order orthogonal Fourier–Mellin moments and geometric correction. Different from classical watermarking algorithms, quantum watermarking algorithms (QWAs) combine principles of quantum computation theory and watermarking strategies [20, 21]. A quantum watermarking scheme was enhanced by utilizing the novel enhanced quantum representation (NEQR) along with a color scrambling technique and small-scale quantum circuits [22]. In order to improve the visual quality and embedding capacity, Zeng et al. [23] proposed a quantum watermarking algorithm by combining the maximal pixel difference with the tent map. A self-recovery QWA was devised with block truncation coding to increase the key space and improve security [24]. In 2021, Li et al. [25] proposed a quantum watermarking scheme for the quantum hue, saturation, and lightness (QHSL) image in the spatial domain. The scheme aimed to protect the integrity and ownership of QHSL images against various attacks. A QWA was presented with the quantum Fourier transformation [26]. Similarly, a quantum image watermarking algorithm was investigated by the quantum Haar wavelet transform [27]. The discrete cosine transform (DCT) is a

Fourier-related transform similar to the discrete Fourier transform but using only **real numbers** [28]. The utilization of DCT shifts an image from the time domain to the frequency domain, where most of the signal information is focused on the low-frequency bands situated in the upper-left corner. DCT is frequently employed for lossy compression, as seen in the JPEG compression of digital images and the MP3 compression of digital audio, owing to its robust energy compaction features. Simultaneously, DCT coefficients in the high-frequency bands, located in the lower-right corner, are nearly zero. Building upon the aforementioned characteristics of the DCT, Mohsen et al. [29] proposed a quantum watermarking algorithm for audio using the quantum discrete cosine transform (QDCT). This algorithm utilizes QDCT, a quantum counterpart of the classical DCT, to achieve enhanced information compression performance inherited from the DCT. Overall, the use of QDCT in audio watermarking offers advantages in terms of imperceptibility and robustness. However, it is important to conduct further research to evaluate the effectiveness and security of QDCT-based QWAs in practical applications and against more sophisticated attacks.

Quantum image scrambling techniques were invented for quantum watermarking due to the superiority of quantum computing models. The quantum Arnold transform is one of the common and available image scrambling methods [30]. However, the risk from the periodicity of the Arnold transform is unavoidable, as attackers can restore the scrambled image with sufficient computing resources. In order to mitigate this risk, a new quantum image scrambling operation using the sinusoidal–tent map is proposed here. This map is a 1D chaotic map which is chosen due to its simple structure and easy implementation. The sinusoidal–tent map exhibits more significant advantages in spatiotemporal performance and chaotic characteristics compared to the sinusoidal map and tent map. Additionally, a quantum color watermarking algorithm is studied by integrating the QDCT with the sinusoidal–tent map, and a quantum network for the proposed quantum image watermark embedding is also devised.

2 Fundamental knowledge

2.1 NCQI model

The NCQI model storing a quantum color image $|I\rangle$ of size $2^n \times 2^n$ was mathematically defined as Eq. 1 [15]

$$|I\rangle = \frac{1}{2^n} \sum_{y=0}^{2^n-1} \sum_{x=0}^{2^n-1} |C(y, x)\rangle \otimes |yx\rangle, \quad (1)$$

where $|C(y, x)\rangle$ denotes the color value of the associated pixel encoded by a binary sequence $R_{q-1} \cdots R_0 G_{q-1} \cdots G_0 B_{q-1} \cdots B_0$ and is expressed as the following Eq. 2.

$$|C(y, x)\rangle = \underbrace{|R_{yx}^{q-1} \cdots R_{yx}^0\rangle}_{\text{Red}} \otimes \underbrace{|G_{yx}^{q-1} \cdots G_{yx}^0\rangle}_{\text{Green}} \otimes \underbrace{|B_{yx}^{q-1} \cdots B_{yx}^0\rangle}_{\text{Blue}}. \quad (2)$$

The grayscale value of each channel R, G , or B ranges from 0 to $2^q - 1$. The NCQI model can store a color image in a normalized quantum superposition state. To represent a pixel, the color

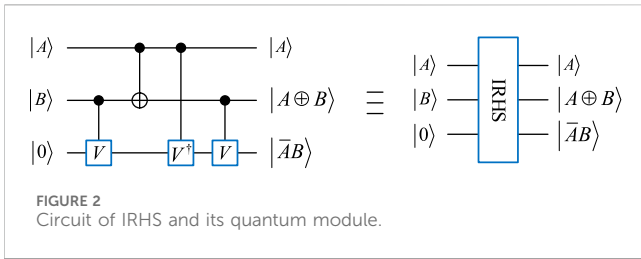


FIGURE 2
Circuit of IRHS and its quantum module.

of RFS, the IRFS module economizes a qubit and one CNOT gate. The IRFS module performs a full-subtraction operation, where the outputs $|A \oplus B \oplus C\rangle$ and $|C(\overline{A \oplus B}) \oplus \overline{AB}\rangle$ denote $|A - B - C\rangle$ and the corresponding borrow bit, respectively. The complexities of quantum circuits of the RFS and IRFS modules are 11 and 10, respectively.

3.1.3 Improved reversible parallel subtractor

A reversible parallel subtractor (RPS) usually involves RHS and RFS [31], and thus the improved reversible parallel subtractor (IRPS) for q -qubit sequences can be implemented by combining IRHS and IRFS. As shown in Figure 4, the sequence $|S\rangle$ denotes the difference between sequence $|X\rangle$ and sequence

$|Y\rangle$. Obviously, the complexities of the single q -qubit IRPS and RPS modules are $10q - 3$ and $11q - 3$, respectively.

3.1.4 Improved calculation of the absolute value

The quantum module CAV consists of RPS and CO [31]. Figure 5 shows the proposed improved calculation of the absolute value (ICAV), which consists of CO and IRPS. A q -qubit CO module is composed of $q + 1$ CNOT gates, one Toffoli gate, and some m -CNOT operation gates.

3.2 Sinusoidal-tent map

3.2.1 Sinusoidal map

The sinusoidal map is a common one-dimensional chaotic map [33] and is defined as Eq. 9.

$$x_{n+1} = ux_n^2 \sin \pi x_n, \tag{9}$$

where $x_n \in (0, 1)$ and u is the control parameter within the range of $u \in (0, 4]$. The bifurcation and Lyapunov exponent plots of the sinusoidal map are shown in Figure 6A; Figure 7A, respectively. The Lyapunov exponents and bifurcation diagram serve as crucial

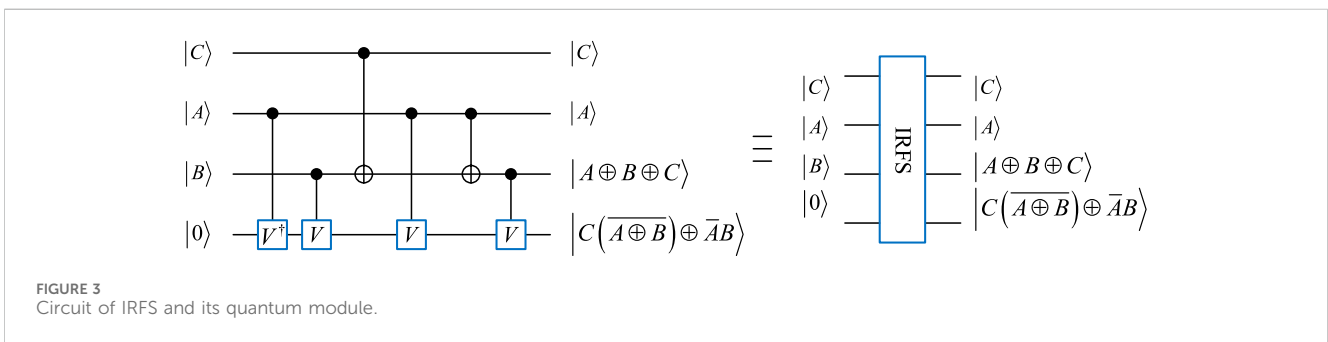


FIGURE 3
Circuit of IRFS and its quantum module.

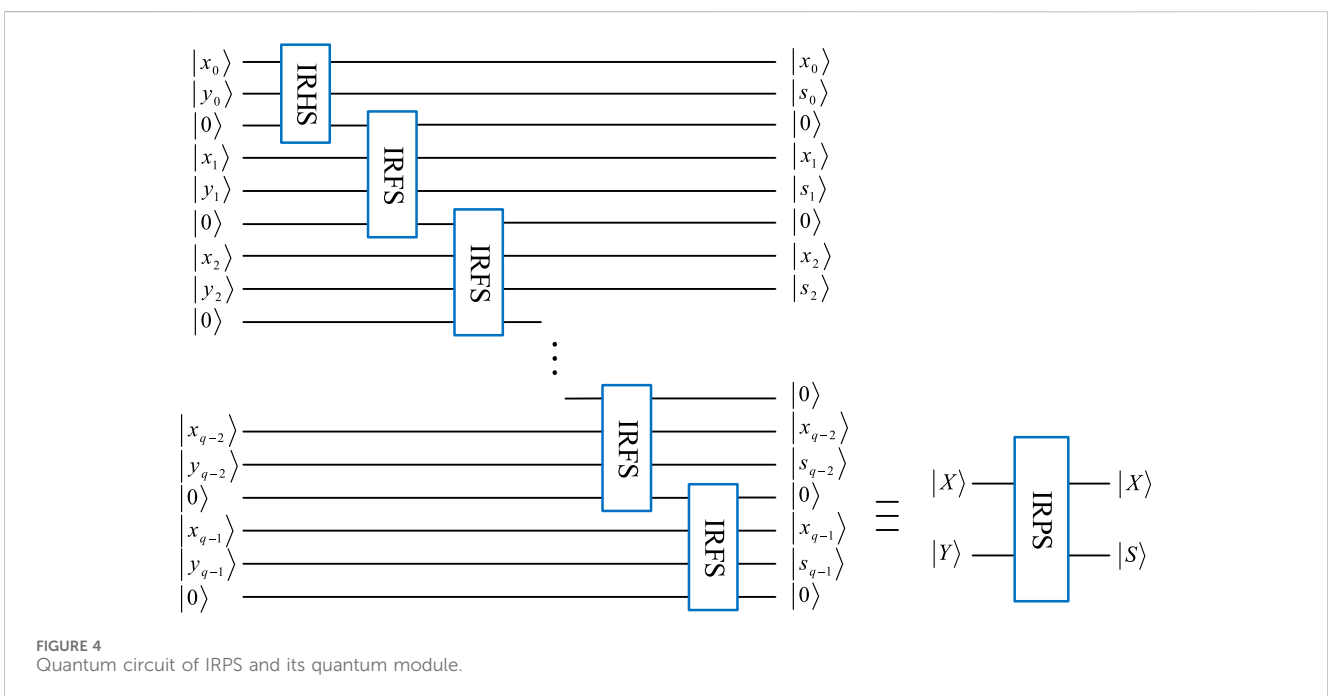


FIGURE 4
Quantum circuit of IRPS and its quantum module.

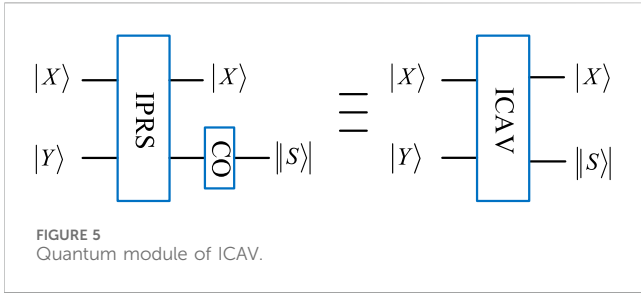


FIGURE 5 Quantum module of ICAV.

metrics in discerning the chaotic characteristics of systems exhibiting chaos. In the case of a chaotic map, the onset of chaotic behavior occurs when its Lyapunov exponents surpass zero. As illustrated in Figure 6A, the Lyapunov exponents of the sinusoidal map exceed 0 only under specific control parameters $u \in [2.16, 2.32]$. Furthermore, as depicted in Figure 7A, the values of the chaotic sequence generated by the sinusoidal map are irregularly distributed within the chaotic range $u \in [2.16, 2.32]$. These observations suggest that the sinusoidal map demonstrates suboptimal chaos behavior, imposing significant limitations on its practical applicability.

3.2.2 Tent map

The tent map is a one-dimensional piece-wise linear map [34] and is defined as Eq. 10.

$$x_{n+1} = \begin{cases} vx_n/2, & x_n < 0.5, \\ v(1-x_n)/2, & x_n \geq 0.5, \end{cases} \quad (10)$$

where $x_n \in (0, 1)$ and v is the parameter within the range of $(0, 4]$. The bifurcation and Lyapunov exponent plots of the tent map are shown in Figure 6B; Figure 7B, respectively. When $v \in [2, 4]$, the tent map is chaotic. Therefore, this mapping also shares the same issues as the sinusoidal mapping technique.

3.2.3 Sinusoidal–tent map

By combining the sinusoidal map with the tent map, a sinusoidal–tent map as the new chaotic map is designed as Eq. 11.

$$x_{n+1} = \begin{cases} [rx_n^2 \sin \pi x_n + 50(0.5 - 20r)x_n] \bmod 1, & x_n < 0.5, \\ [rx_n^2 \sin \pi x_n + 50(0.5 - 20r)(1 - x_n)] \bmod 1, & x_n \geq 0.5, \end{cases} \quad (11)$$

where the parameter $r \in (0, 4]$ and x_n is the output chaotic sequence. Compared with the sinusoidal and tent maps, the designed sinusoidal–tent map performs better in terms of bifurcation

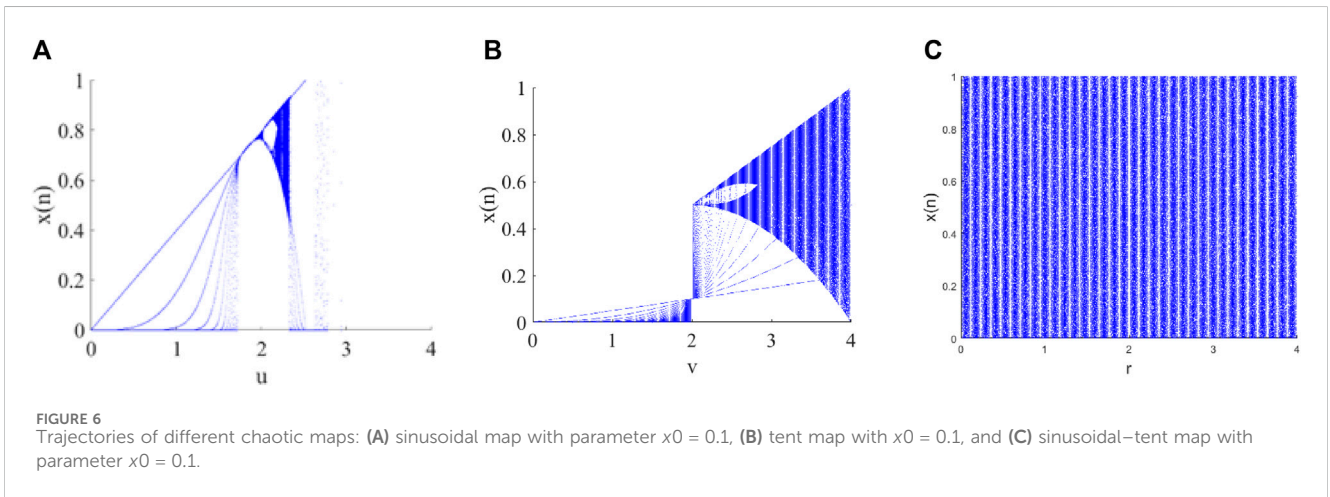


FIGURE 6 Trajectories of different chaotic maps: (A) sinusoidal map with parameter $x_0 = 0.1$, (B) tent map with $x_0 = 0.1$, and (C) sinusoidal–tent map with parameter $x_0 = 0.1$.

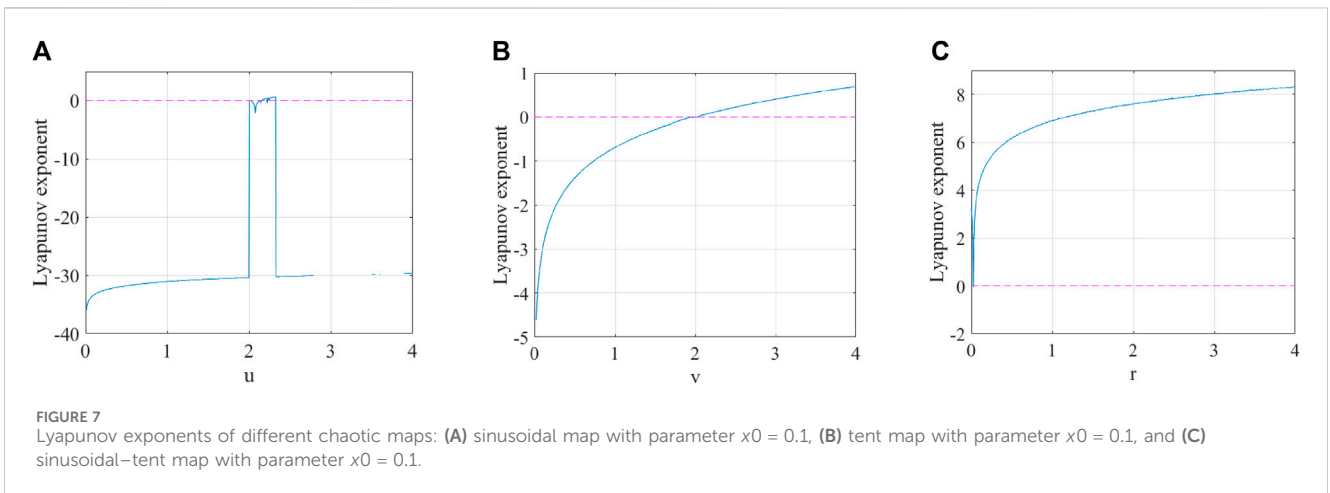


FIGURE 7 Lyapunov exponents of different chaotic maps: (A) sinusoidal map with parameter $x_0 = 0.1$, (B) tent map with parameter $x_0 = 0.1$, and (C) sinusoidal–tent map with parameter $x_0 = 0.1$.

diagram and Lyapunov exponents. As shown in Figure 6, the bifurcation of ST is distributed across the entire data range of the plane. This distribution area is significantly larger than the outputs of the sinusoidal map and tent map. By observing Figure 7, it can be noted that the Lyapunov exponents of the ST map are all positive within the range of control parameters, indicating favorable chaotic characteristics.

3.3 Quantum scrambling with the sinusoidal–tent map

The Arnold scrambling method is insecure with sufficient computing resources owing to its periodicity. Therefore, we put forward a new irregular scrambling method. The scrambling on a quantum image $|K\rangle = \frac{1}{2^n} \sum_{y=0}^{2^n-1} \sum_{x=0}^{2^n-1} \otimes |D_{yx}^j\rangle |yx\rangle$ is as follows:

(1) a and b are chosen as initial parameter values of the sinusoidal–tent map. Then, two chaotic sequences $\{x_{1i}|i = 0, 1, \dots, j\}$ and $\{x_{2i}|i = 0, 1, \dots, j\}$ are generated using the sinusoidal–tent map, where j represents the j th iteration. Then, the two chaotic sequences are converted into integer sequences $\{h_i^*|i = 0, 1, \dots, j\}$ and $\{l_i^*|i = 0, 1, \dots, j\}$, respectively, which are represented as Eq. 12 and Eq. 13.

$$h_i^* = \text{floor}(\text{mod}(x_{1i} \times 10^{15}, 2^n)), \tag{12}$$

$$l_i^* = \text{floor}(\text{mod}(x_{2i} \times 10^{15}, 2^n)). \tag{13}$$

(2) The original image is then scrambled via the element values of $|h_i^*\rangle$ and $|l_i^*\rangle$, where $|h_i^*\rangle$ and $|l_i^*\rangle$ express the quantum states of sequences $\{h_i^*|i = 0, 1, \dots, j\}$ and $\{l_i^*|i = 0, 1, \dots, j\}$, respectively. The quantum image position scrambling operation is denoted as S , and the $2^n \times 2^n$ scrambled image $|K_S\rangle$ is represented as Eq. 14.

$$\begin{aligned} |K_S\rangle &= S|K\rangle = \frac{1}{2^n} \sum_{y=0}^{2^n-1} \sum_{x=0}^{2^n-1} \otimes_{i=0}^{q-1} |D_{yx}^j\rangle S|yx\rangle \\ &= \frac{1}{2^n} \sum_{y=0}^{2^n-1} \sum_{x=0}^{2^n-1} \otimes_{i=0}^{q-1} |D_{yx}^j\rangle |y_S x_S\rangle, \end{aligned} \tag{14}$$

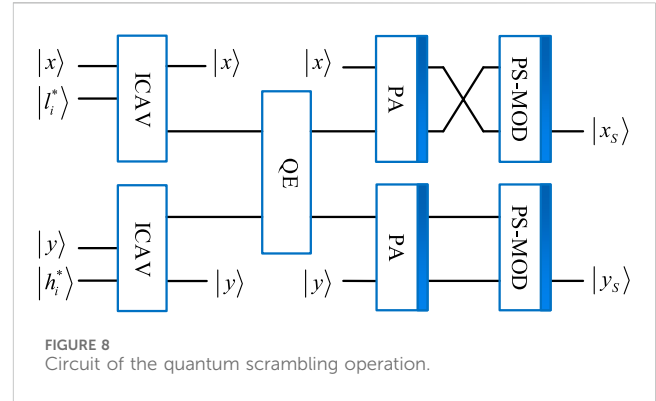
where $|y_S x_S\rangle = |y_S\rangle |x_S\rangle = (|y\rangle - |h_i^*\rangle \text{mod } 2^n)(|x\rangle - |l_i^*\rangle \text{mod } 2^n)$ and $|*|$ represents the absolute value operation. The quantum module of this scrambling operation is shown in Figure 8.

3.4 Watermark embedding procedure

During the watermark embedding process, the color image I is watermarked with a binary watermark W . Figure 9 shows the embedding procedure of the quantum color image watermarking algorithm, and the detailed embedding process is given below.

Step 1: The classical image I of size $2^n \times 2^n$ is transformed into a quantum image $|I\rangle$ by the NCQI.

Step 2: With the initial parameter value a of the sinusoidal–tent map, one chaotic sequence $\{x_{1i}|i = 0, 1, \dots, j\}$ is produced using the sinusoidal–tent chaotic map. The chaotic sequence



$\{x_{1i}|i = 0, 1, \dots, j\}$ is changed to an integer sequence $\{x'_i|i = 0, 1, \dots, j\}$:

$$x'_i = \text{floor}(\text{mod}(x_{1i} \times 10^{15}, 256)), \tag{15}$$

$$x''_i = x'_i \text{mod } 3. \tag{16}$$

According to Eq. 16, if x''_i equals to 0, 1, or 2, then R, G, or B channel of the quantum image $|I\rangle$ is chosen to embed the watermarking image, i.e., $|P\rangle$.

Step 3: The original watermark W of size $2^n \times 2^n$ is transformed into a quantum image $|W\rangle$ by the NEQR. Then, a scrambled quantum watermarked image $|W'\rangle$ is yielded by executing the quantum scrambling operation S on $|W\rangle$. The quantum scrambling circuit is shown in Figure 8.

Step 4: Image $|P\rangle$ is translated into the frequency domain by the QDCT operation. The energy of the QDCT coefficients is mainly congregated in the upper-left corner of the sub-block, which is the low-frequency part of an image, and most of the remaining coefficients are very close to zero. Therefore, the medium-frequency part is a better area to embed the watermark compared with the low-frequency part. $|P'\rangle$ is an image transformed using the QDCT operation.

Step 5: The medium-frequency QDCT coefficients of every sub-block are selected randomly and embedded with a quantum image $|W'\rangle$ multiplied by a coefficient k to obtain $|P^*\rangle$ by Eq. 17:

$$|P^*\rangle = |P'\rangle + k|W'\rangle. \tag{17}$$

Step 6: After executing the inverse QDCT on $|P^*\rangle$ to obtain $|P''\rangle$, the final color image $|I^*\rangle$ inserted with a secret message can be yielded from the reconstructed $|P''\rangle$ and other channels.

A quantum watermark embedding network is shown in Figure 10, where $|Y\rangle = |y_{n-1}y_{n-2}\dots y_0\rangle$ and $|X\rangle = |x_{n-1}x_{n-2}\dots x_0\rangle$. $E(k)$ denotes the scrambled quantum watermarked image $|W'\rangle$ multiplied by the watermark embedding coefficient k .

3.5 Watermark extraction

The watermark image is extracted from a watermarked quantum color image with the help of the color host image and the keys to choose the embedded channel and scramble the watermark image.

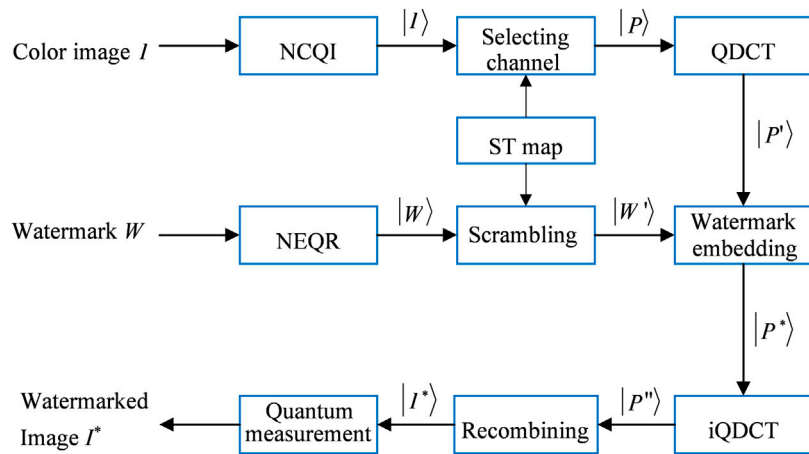


FIGURE 9 Embedding procedure of the quantum watermarking algorithm.

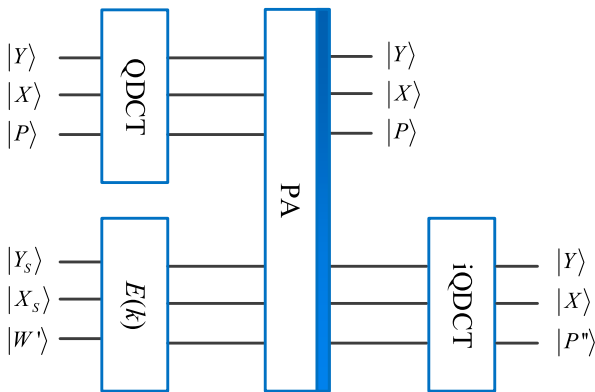


FIGURE 10 Quantum watermark embedding network.

Figure 11 shows the extraction of the designed quantum color image watermarking algorithm, and the extraction process is detailed below.

Step 1: First, in order to extract the watermark image from the host image, the classical watermarked image I^* should be transformed into the corresponding quantum state $|I^*\rangle$ by the NCQI.

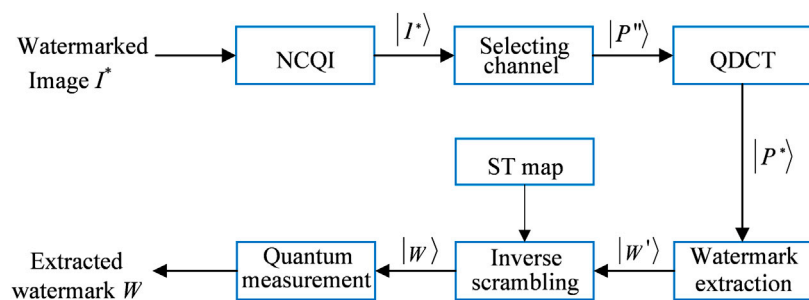


FIGURE 11 Extraction procedure of the quantum watermarking algorithm.

Step 2: The chaotic sequence $\{x_{1i}|i = 0, 1, \dots, j\}$ is generated by the sinusoidal–tent map with the same initial parameter a . According to Eq. 15 and Eq. 16, the random sequence x_{1i} is converted into the random integer sequence x''_{1i} . In the following, if x''_{1i} equals to 0, 1, or 2, the corresponding R, G, or B channel $|P''\rangle$ with a watermark image can be easily chosen from the final color image $|I^*\rangle$.

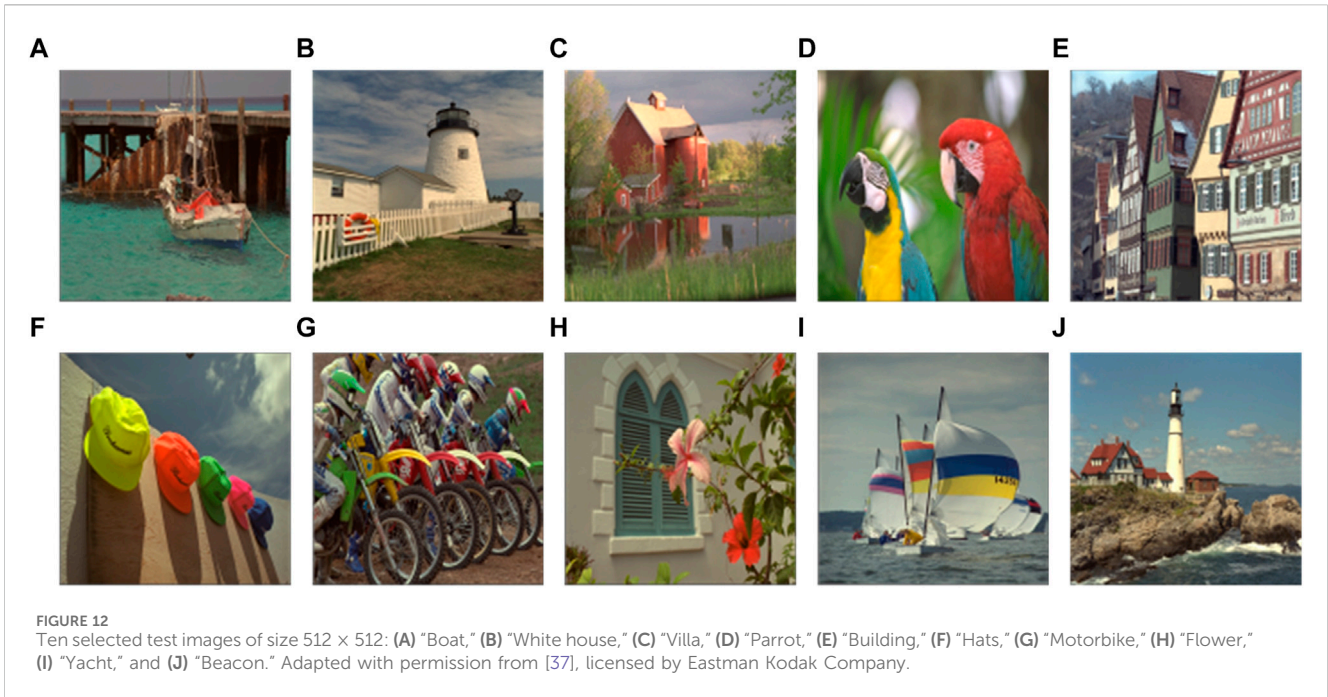
Step 3: This step is only to perform QDCT on the watermarked image $|P''\rangle$ in order to recover the quantum image $|P^*\rangle$.

Step 4 : $|P^l\rangle$ can be obtained by performing the QDCT operation on image $|P\rangle$. According to the corresponding medium-frequency embedding position, the scrambled watermark image $|W'\rangle$ could be obtained as Eq. 18.

$$|W'\rangle = (|P^*\rangle - |P^l\rangle) / k. \tag{18}$$

Step 5: The sequences $\{h_i^*|i = 0, 1, \dots, j\}$ and $\{l_i^*|i = 0, 1, \dots, j\}$ are then generated using the sinusoidal–tent map controlled by the initial parameters a and b , respectively. By recalling $|h_i^*\rangle$ and $|l_i^*\rangle$, the extracted watermark image $|W\rangle$ is acquired by executing the inverse scrambling operation S^{-1} shown in Eq. 19:

$$|W\rangle = S^{-1}|W'\rangle = S^{-1}S|W\rangle. \tag{19}$$



Step 6: After quantum measurement, the quantum watermark image $|W\rangle$ is eventually translated into a classical image.

4 Numerical simulation and discussion

The numerical simulations are carried out under the MATLAB R2017b platform on a classical PC. Ten host color images of size 512 × 512 taken for the test are shown in Figure 12. Two binary watermark images of sizes 128 × 128 and 64 × 64 are shown in Figure 13. The initial values a and b and the control parameter r of the sinusoidal–tent map are set to 0.325, 0.333, and 0.1, respectively, and the embedding coefficient k of the proposed color image QWA is set at 0.01.

The scrambling operation S is executed on the watermark image "Camera" and "Cat," and Figures 14A, B show the corresponding scrambled watermark images. As shown in Figure 14, the proposed scrambling operation has an acceptable scrambling performance.

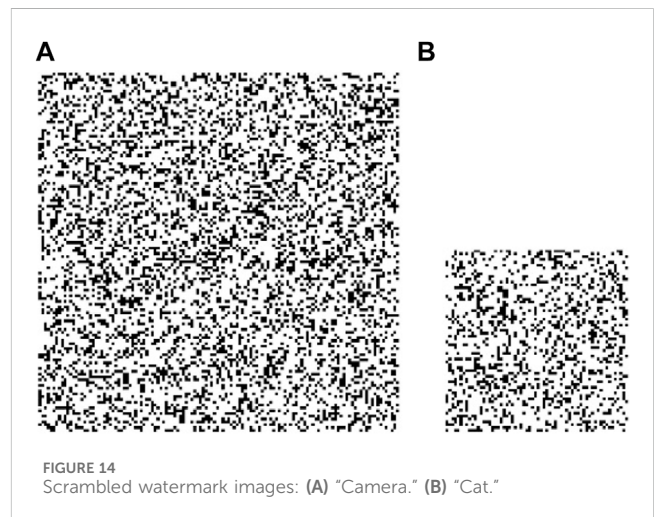
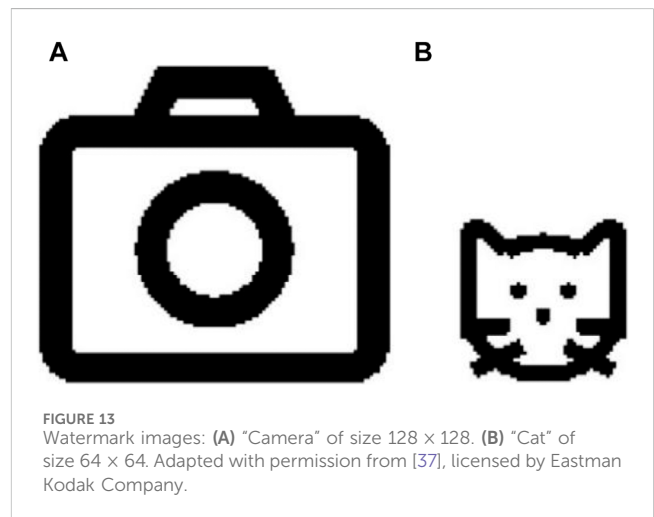
4.1 Watermark evaluation exponents

The peak signal-to-noise ratio (PSNR) is expressed as Eq. 20.

$$PSNR = 20 \lg \frac{2^n - 1}{MSE}, \tag{20}$$

where $2^n - 1$ is the maximal image grayscale value, $MSE = \frac{1}{N} \sum_{e,r} [I(e,r) - Z(e,r)]^2$ is the mean-squared error between the host image $I(e,r)$ and its associated watermarked image $Z(e,r)$, and N is the number of pixels in an image.

The structural similarity exponent matrix (SSIM) can assess the distortion of an image or the similarity of two images according to Eq. 21:



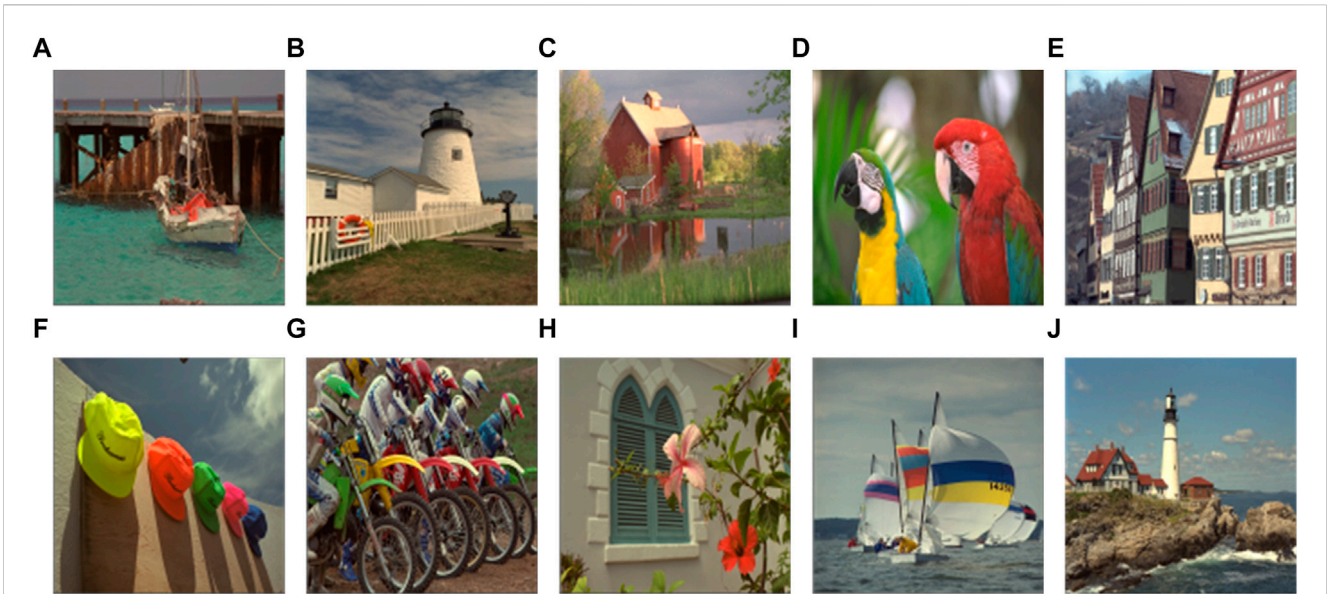


FIGURE 15 Watermarked image with "Camera": (A) "Boat," (B) "White house," (C) "Villa," (D) "Parrot," and (E) "Building." Watermarked image with "Cat": (F) "Hats," (G) "Motorbike," (H) "Flower," (I) "Yacht," and (J) "Beacon." Adapted with permission from [37], licensed by Eastman Kodak Company.

$$SSIM(x, y) = \frac{(2\mu_x\mu_y + c_1)(2\sigma_{xy} + c_2)}{(\mu_x^2 + \mu_y^2 + c_1)(\sigma_x^2 + \sigma_y^2 + c_2)} \quad (21)$$

where c_1 and c_2 are constants, σ and μ are the variance value and the mean value, respectively, and σ_{xy} is the covariance value of x and y .

Normalized cross-correlation (NCC) is another important exponent to assess the similarity of two images and is usually employed to measure the robustness of watermarking algorithms against different attacks, which is expressed as Eq. 22.

$$NCC(I, Z) = \frac{\sum_{x=1}^M \sum_{y=1}^N [I(x, y) - \mu_I][Z(x, y) - \mu_Z]}{\sqrt{\sum_{x=1}^M \sum_{y=1}^N [I(x, y) - \mu_I]^2} \sqrt{\sum_{x=1}^M \sum_{y=1}^N [Z(x, y) - \mu_Z]^2}} \quad (22)$$



Here, $M \times N$ is the image size. $I(x, y)$ and $Z(x, y)$ represent the pixel values of images I and Z at the position (x, y) , respectively. The NCC value is in the range of $[-1, 1]$. The closer the NCC value is to 1, the more similar the two images are.

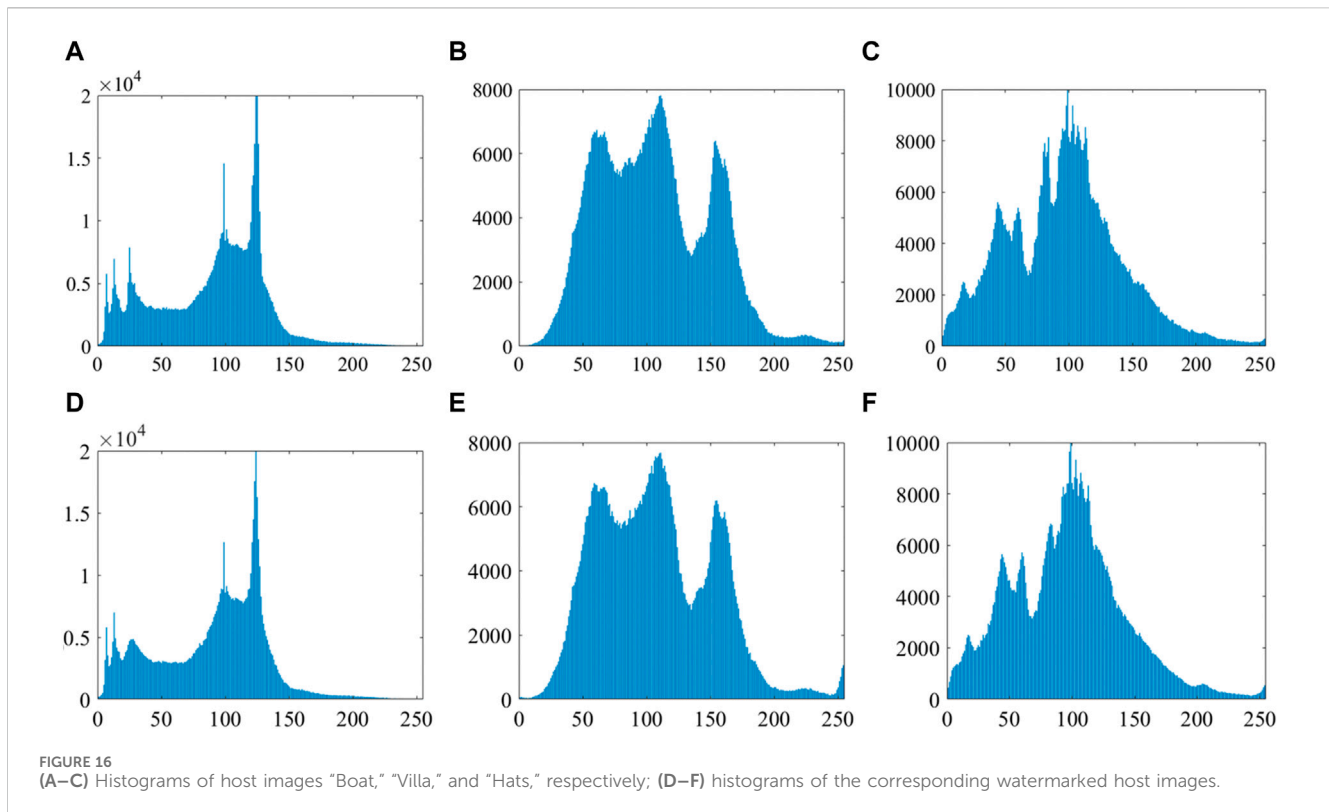
4.2 Imperceptibility analysis

Figures 15A–E show the watermarked color images with the watermark image "Camera," while Figures 15F–I show the watermarked images with the watermark image "Cat." By observing and comparing Figure 12; Figure 15, it can be observed that there is no significant difference between the watermarked image and the original host image.

The values listed in Table 1 represent the PSNR and SSIM for the watermark image with two different sizes. The PSNR is mainly used

TABLE 1 PSNR and SSIM values with the proposed QWA.

Watermark image	Host image	PSNR	SSIM
Camera 128×128 	Boat	48.24	0.9974
	House	46.11	0.9965
	Villa	46.78	0.9967
	Parrot	46.06	0.9980
	Building	45.94	0.9987
	Hats	46.73	0.9976
	Motorbike	48.39	0.9992
	Flower	46.38	0.9976
	Yacht	45.68	0.9919
	Beacon	47.26	0.9978
Cat 64×64 	Boat	54.18	0.9995
	House	51.80	0.9992
	Villa	52.32	0.9990
	Parrot	51.87	0.9995
	Building	51.56	0.9996
	Hats	52.56	0.9994
	Motorbike	53.90	0.9998
	Flower	52.58	0.9995
	Yacht	51.83	0.9985
	Beacon	53.44	0.9996



for the evaluation and comparison of image and video compression algorithms and can help measure the impact of different compression algorithms on the quality of images or videos. The higher the value of the PSNR, the smaller the difference between two images, indicating higher quality. Generally, if the PSNR value is greater than 30 dB, it is hard to differentiate between the original host image and the watermarked image. If the PSNR value is greater than 40 dB, then the invisibility of the image watermark algorithm can be ensured. As for the watermark images “Camera” and “Cat,” the average PSNR values of the host image and the watermarked image with the proposed QWA are 46.76 dB and 52.60 dB, respectively. It indicates that the quality of the watermarked image and the corresponding original host image are very close. In addition, the SSIM values of the host image and the watermarked one approach 1. The SSIM value ranges from 0 to 1, where 1 indicates that the two images are identical and 0 indicates that the two images are completely different. A higher SSIM value indicates that the two images are more similar. Therefore, the proposed color image watermark algorithm has good invisibility.

In image processing, histograms are valuable tools for analyzing various image features, such as contrast, brightness, and color distribution. By comparing histograms of different images, we can determine their similarities or differences. For instance, if the histograms of two images are closely matched, it suggests that they may have comparable color distributions, indicating their similarity. In Figure 16, the histogram of the watermarked image is similar to the histogram of the original carrier image. This implies that the pixel intensity distributions of the two images may be similar. This can be considered evidence that the watermark image has been successfully embedded into the original carrier image without significantly altering the pixel distribution characteristics of the

images. Figures 16A–C show the histograms of three selected host images: “Boat,” “Villa,” and “Hats,” respectively. Figures 16D–F show the histograms of the associated watermarked images. In Figure 16, the histogram of the watermarked image closely resembles that of the original carrier images. This similarity implies that the pixel intensity distributions of the two images may be comparable. Thus, this similarity serves as evidence that the watermark image has been successfully embedded into the original carrier image without significantly altering its pixel distribution characteristics.

4.3 Robustness analysis

The image “Cat” of size 64×64 and image “Boat” of size 512×512 are treated as the watermark image and host image, respectively. As shown in Figure 17, there are no significant difference between the watermarked image and the original host image and no significant distinction between the extracted watermark image and the original watermark image. Noise attack, JPEG compression attack, and filtering attack are used to test the robustness of this algorithm.

4.3.1 Noise attack

Noise attack is a common method used to test the robustness of algorithms against the addition of noise in images. By conducting noise attack tests, the robustness of image processing algorithms against different intensities and types of noise can be evaluated. Salt-and-pepper noise with densities of 0.01, 0.03, and 0.05 was added to the watermarked image “Boat.” The watermarked images, along with the corresponding extracted watermark images containing the respective noises, are shown in Figure 18. The

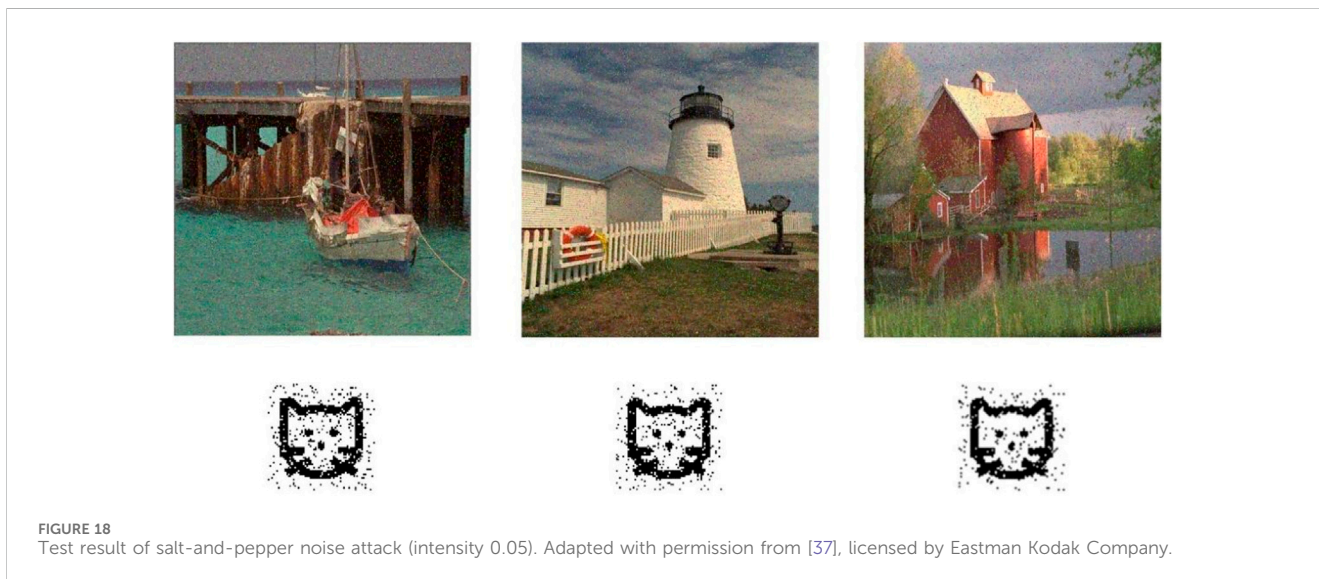
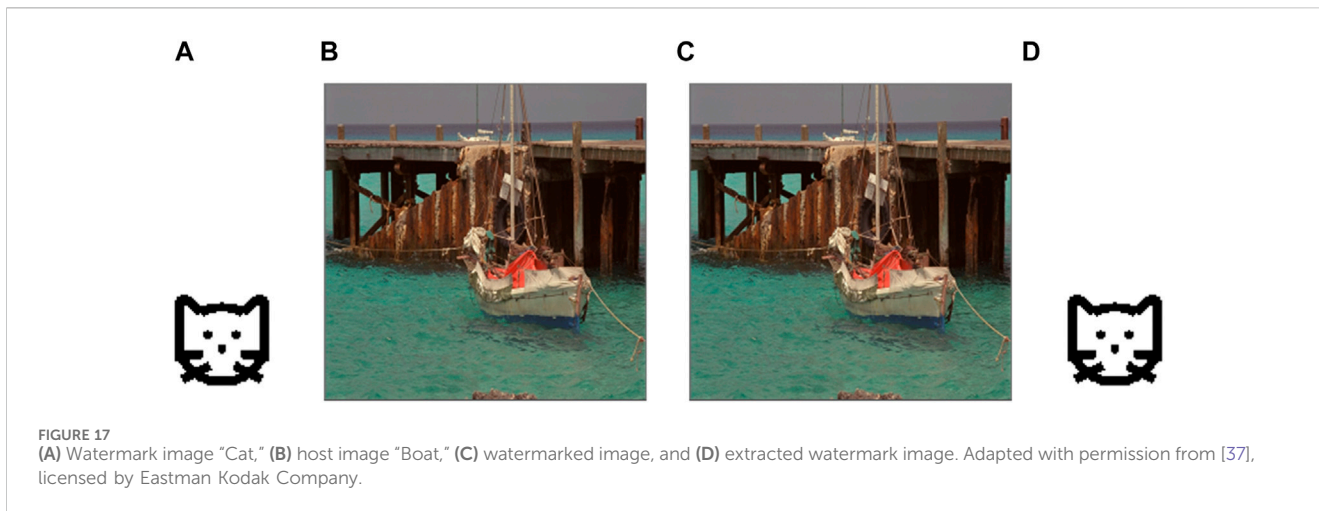


TABLE 2 Test results of salt-and-pepper noise attack.

Salt-and-pepper noise intensity	NCC value		
	Boat	House	Villa
0.01	0.9787	0.9720	0.9854
0.03	0.9640	0.9612	0.9679
0.05	0.9498	0.9432	0.9613

TABLE 3 Test results of JPEG compression attack.

JPEG compression	NCC value		
	Boat	House	Villa
QF = 90	0.9987	0.9952	0.9959
QF = 70	0.9950	0.9912	0.9915
QF = 50	0.9921	0.9884	0.9873

NCC values of the extracted watermark images with the added noises are shown in Table 2. From Table 2, it can be observed that the proposed QWA performs well in terms of withstanding noise attacks.

4.3.2 JPEG compression attack

A JPEG compression attack refers to applying different intensities of JPEG compression to an image with an embedded watermark and evaluating the watermark extraction effectiveness in the compressed image. The experimental results of JPEG compression attacks are

shown in Table 3. Quality factor parameters used for JPEG compression in the experiment are set to 90, 70, and 50, respectively. Figure 19 shows the watermarked images subjected to different intensities of JPEG compression attacks, along with the corresponding extracted watermark images. Notably, even when the quality factor parameter was set to 50, the extracted watermark images remained complete and clear, with all corresponding NCC values exceeding 0.98. As a result, the presented quantum color image watermarking algorithm demonstrates resistance against JPEG compression attacks.

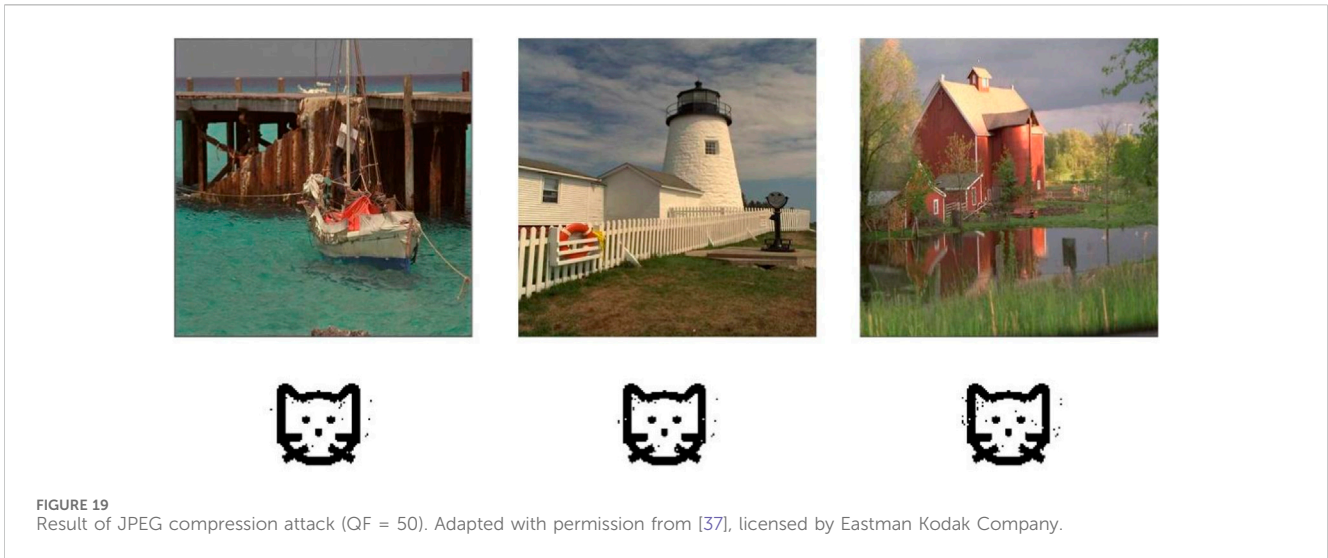


FIGURE 19 Result of JPEG compression attack (QF = 50). Adapted with permission from [37], licensed by Eastman Kodak Company.

TABLE 4 Test results of filtering attack.

Watermark image	Boat	House	Villa
Extracted watermark			
NCC value	0.9945	0.9918	0.9901

TABLE 5 PSNR values calculated using the proposed scheme and previous works.

Host image	[21]	[35]	[36]	Proposed scheme
Strength k	0.01	1	0.01	0.01
Watermark size	64 × 64	32 × 32	64 × 64	64 × 64
Average value	51.466	37.2960	30.4624	52.3460

TABLE 6 SSIM values calculated using the proposed scheme and previous works.

Host image	[21]	[35]	[36]	Proposed scheme
Strength k	0.01	1	0.01	0.01
Watermark size	64 × 64	32 × 32	64 × 64	64 × 64
Average value	0.9800	0.9432	0.9371	0.9994

4.3.3 Filtering attack

A filtering attack refers to a type of cyber-attack in which an attacker tries to block or filter out certain information or content from reaching its intended recipient. The median filtering with a filtering window 3×3 is exploited to interfere with the watermarked image. Table 4 shows the watermark images extracted from the host images under filtering attack and the corresponding NCC values. The NCC values corresponding to the extracted watermark image are all above 0.99. As a result, the proposed color image QWA can resist filtering attacks.

enhancement in imperceptibility within the proposed algorithm is attributed to the strategic embedding of the watermark into the medium-frequency component of the transformed host image. By focusing on this frequency range, the QWA achieves a balance between robust watermark insertion and minimizing perceptual impact, thereby ensuring an improved level of invisibility compared to the referenced algorithms. The utilization of the medium-frequency component allows the proposed QWA to maintain the visual quality of the watermarked image while successfully concealing the embedded information.

4.4 Comparative analysis

The imperceptibility of the proposed QWA compared with other typical algorithms [21, 35, 36] is shown in Tables 5, 6. Notably, the QWA exhibits superior performance with PSNR and SSIM values when compared to the algorithms referenced in [21, 35, 36]. This

4.5 Quantum circuit complexity analysis

The complexity of our proposed color image QWA is mainly related to the quantum scrambling operation and the QDCT. The presented quantum scrambling operation can be realized with two ICAV modules, one QE module, two PA modules, and two PS-MOD

modules. For an image of size $2^q \times 2^q$, the complexity of a q -qubit ICAV module is $12q^2 - 45q + 28$. The QE module involves $2q$ CNOT gates and a q -CNOT gate, so its complexity is $6q - 8$. The complexity of PA and PS-MOD is $O(q)$. Apparently, the complexity of the scrambling operation is $O(q^2)$. For an image of size $2^n \times 2^n$, the computing complexity of the QDCT is $O(2^n)$. To sum up, the complexity of the proposed color image QWA is $O(2^n)$.

5 Conclusion and future challenges and directions

5.1 Conclusion

A one-dimensional chaotic map, i.e., a sinusoidal–tent map, is devised by combining the sinusoidal map with the tent map. Depending on the random sequence generated using the sinusoidal–tent map, a new position scrambling operation on a quantum image together with the associated quantum circuit is devised. The original quantum circuits of some existing quantum modules are improved to reduce their complexities. The security of QWA is enhanced by using the sinusoidal–tent map to scramble the watermark image. After the quantum discrete cosine transform, most of the signal energy is concentrated on the low-frequency part; thus, choosing the medium-frequency component to embed watermark can enhance the invisibility and robustness of the algorithm. The experimental results illustrate that the QWA has good invisibility and high robustness against noise attack, JPEG compression attack, and filtering attack.

5.2 Potential future challenges and directions

Currently, the quantum watermark technology is generally implemented by simulating quantum theory on classical computers, and there are no well-developed quantum devices available for testing. Therefore, future challenges lie in continuously adjusting the direction of quantum watermark algorithms to cater to the development of quantum computers. This will require proposing algorithms that are better suited for quantum computer applications. Therefore, the future research directions for quantum watermarking will focus on algorithm development, physical implementation, robustness analysis, and application expansion. By exploring these areas, we can create more opportunities and face new challenges in protecting digital content, enhancing information security, and advancing quantum technology.

References

- Velayatipour M, Mosleh M, Nejad MY, Kheyrandish M. Quantum reversible circuits for audio watermarking based on echo hiding technique. *Quan Inf Process* (2022) 21(9):316. doi:10.1007/s11128-022-03657-9
- Liang Q, Zhu CX. A new one-dimensional chaotic map for image encryption scheme based on random dna coding. *Opt Laser Technol* (2023) 160:109033. doi:10.1016/j.optlastec.2022.109033
- Zhou NR, Hu LL, Huang ZW, Wang MM, Luo GS. Novel multiple color images encryption and decryption scheme based on a bit-level extension algorithm. *Expert Syst Appl* (2023) 238:122052. doi:10.1016/j.eswa.2023.122052
- Huang ZW, Zhou NR. Image encryption scheme based on discrete cosine Stockwell transform and DNA-level modulus diffusion. *Opt Laser Technol* (2022) 149:107879. doi:10.1016/j.optlastec.2022.107879
- Zhou NR, Tong LJ, Zou WP. Multi-image encryption scheme with quaternion discrete fractional Tchebyshev moment transform and cross-coupling operation. *Signal Process*. (2023) 211:109107. doi:10.1016/j.sigpro.2023.109107
- Leong K, Sung A. What business managers should know about quantum computing? *J Interdiscip Sci* (2022) 6(2):42–52.

Data availability statement

The datasets presented in this article are not readily available. The data and implementation code for MATLAB are available upon request. Requests to access the datasets should be directed to ppzeng@ncu.edu.cn.

Author contributions

P-PZ: conceptualization, funding acquisition, investigation, methodology, validation, and writing—original draft. XZ: formal analysis, software, and writing—original draft. D-FZ: data curation, visualization, and writing—review and editing. S-HC: data curation, validation, and writing—review and editing. L-HG: project administration, supervision, validation, and writing—review and editing.

Funding

The author(s) declare that financial support was received for the research, authorship, and/or publication of this article. This work was supported by the National Natural Science Foundation of China (Grant Nos 62202252 and 61861029), the Science and Technology Planning Project of Shanghai (Grant No. 23010501800), the Science and Technology Research Project of Jiangxi Education Department (GJJ2203915), and the Higher Education Reformation Project of Jiangxi Province (JXJG-22-30-5).

Conflict of interest

The authors declare that the research was conducted in the absence of any commercial or financial relationships that could be construed as a potential conflict of interest.

Publisher's note

All claims expressed in this article are solely those of the authors and do not necessarily represent those of their affiliated organizations, or those of the publisher, the editors, and the reviewers. Any product that may be evaluated in this article, or claim that may be made by its manufacturer, is not guaranteed or endorsed by the publisher.

7. Beach G, Lomont C, Cohen C. Quantum image processing (QuIP). In: 32nd Applied Imagery Pattern Recognition Workshop; 15-17 October 2003; Washington, DC, USA (2003). p. 39–44.
8. Li HS, Fan P, Xia HY, Peng H, Long GL. Efficient quantum arithmetic operation circuits for quantum image processing. *Sci China: Phys Mech Astron* (2020) 63(8):280311. doi:10.1007/s11453-020-1582-8
9. Ali AE, Abdel-Galil H, Mohamed S. Quantum image mid-point filter. *Quan Inf Process* (2020) 19(8):238. doi:10.1007/s11128-020-02738-x
10. Le PQ, Dong FY, Hirota K. A flexible representation of quantum images for polynomial preparation, image compression, and processing operations. *Quan Inf Process* (2011) 10(1):63–84. doi:10.1007/s11128-010-0177-y
11. Zhang Y, Lu K, Gao YH, Wang M. NEQR: a novel enhanced quantum representation of digital images. *Quan Inf Process* (2013) 12(8):2833–60. doi:10.1007/s11128-013-0567-z
12. Yuan SZ, Mao X, Xue YL, Chen L, Xiong Q, Compare A. SQR: a simple quantum representation of infrared images. *Quan Inf Process* (2014) 13(6):1353–79. doi:10.1007/s11128-014-0733-y
13. Yan F, Iliyasu AM, Venegas-Andraca SE. A survey of quantum image representations. *Quan Inf Process* (2016) 15(1):21–35. doi:10.1007/s11128-015-1195-6
14. Jiang N, Wang J, Mu Y. Quantum image scaling up based on nearest-neighbor interpolation with integer scaling ratio. *Quan Inf Process* (2015) 14(11):4001–26. doi:10.1007/s11128-015-1099-5
15. Sang JZ, Wang S, Li Q. A novel quantum representation of color digital images. *Quan Inf Process* (2017) 16(2):42. doi:10.1007/s11128-016-1463-0
16. Zhu HH, Chen XB, Yang YX. A multimode quantum image representation and its encryption scheme. *Quan Inf Process* (2021) 20(9):315. doi:10.1007/s11128-021-03255-1
17. Wang L, Ran QW, Ma J. Double quantum color images encryption scheme based on DQRCL. *Multimedia Tools Appl* (2020) 79(9):6661–87. doi:10.1007/s11042-019-08514-z
18. Sencar HT, Ramkumar M, Akansu AN. *Data hiding fundamentals and applications: content security in digital multimedia*. San Diego, CA, USA: Academic Press (2004).
19. Gong LH, Luo HX. Dual color images watermarking scheme with geometric correction based on quaternion FrOOFMMs and LS-SVR. *Opt Laser Technol* (2023) 167:109665. doi:10.1016/j.optlastec.2023.109665
20. Zhou NR, Luo AW, Zou WP. Secure and robust watermark scheme based on multiple transforms and particle swarm optimization algorithm. *Multimedia Tools Appl* (2019) 78:2507–23. doi:10.1007/s11042-018-6322-9
21. Wang MX, Yang HM, Jiang DH, Yan B, Pan JS, Wang T. A novel quantum image watermarking scheme for tamper localization and self-recovery. *Quan Inf Process* (2022) 21(8):277. doi:10.1007/s11128-022-03619-1
22. Li PC, Zhao Y, Xiao H, Cao M. An improved quantum watermarking scheme using small-scale quantum circuits and color scrambling. *Quan Inf Process* (2017) 16(5):127. doi:10.1007/s11128-017-1577-z
23. Zeng QW, Wen ZY, Fu JF, Zhou NR. Quantum watermark algorithm based on maximum pixel difference and tent map. *Int J Theor Phys* (2021) 60(9):3306–33. doi:10.1007/s10773-021-04909-7
24. Hemida O, He H. A self-recovery watermarking scheme based on block truncation coding and quantum chaos map. *Multimed Tools Appl* (2020) 79(25):18695–725. doi:10.1007/s11042-020-08727-7
25. Li NQ, Yan F, Hirota K. Quantum watermarking schemes for QHSL images in spatial domain. 2021 8th international conference on soft computing and machine intelligence (ISCM). *Cairo, Egypt* (2021) 225–30. doi:10.1109/ISCM53840.2021.9654956
26. Zhang WW, Gao F, Liu B, Wen QY, Chen H. A watermark strategy for quantum images based on quantum Fourier transform. *Quan Inf Process* (2013) 12(2):793–803. doi:10.1007/s11128-012-0423-6
27. Zeng QW, Ge HY, Fu JF, Gong L, Zou W. Quantum watermarking algorithm based on quantum Haar wavelet transform and Henon map. *Int J Theor Phys* (2022) 61(6):167. doi:10.1007/s10773-022-04998-y
28. Ahmed N, Natarajan T, Rao KR. Discrete cosine transform. *IEEE Trans Comput* (1974) C-23(1):90–3. doi:10.1109/t-c.1974.223784
29. Mohsen YN, Mohammad M, Saeed RH. A blind quantum audio watermarking based on quantum discrete cosine transform. *J Inf Security Appl* (2020) 55:102495. doi:10.1016/j.jisa.2020.102495
30. Liu XB, Xiao D, Liu C. Three-level quantum image encryption based on Arnold transform and logistic map. *Quan Inf Process* (2021) 20(1):23. doi:10.1007/s11128-020-02952-7
31. Zhou RG, Hu WW, Luo GF, Liu X, Fan P. Quantum realization of the nearest neighbor value interpolation method for INEQR. *Quan Inf Process* (2018) 17(7):166. doi:10.1007/s11128-018-1921-y
32. Zhou RG, Hu WW, Fan P. Quantum watermarking scheme through Arnold scrambling and LSB steganography. *Quan Inf Process* (2017) 16(9):212. doi:10.1007/s11128-017-1640-9
33. Ahmed A, Sridevi S, Hayder K, Ahmadi A, Rajagopal K, Jafari S. A novel multi-stable sinusoidal chaotic map with spectacular behaviors. *Commun Theor Phys* (2023) 75:115001. doi:10.1088/1572-9494/acf307
34. Zhou YC, Long B, Chen CL. A new 1D chaotic system for image encryption. *Signal Process*. (2014) 97:172–82. doi:10.1016/j.sigpro.2013.10.034
35. Su QT, Liu DC, Yuan ZH, Wang G, Zhang X, Chen B, et al. New rapid and robust color image watermarking technique in spatial domain. *IEEE Access* (2019) 7(3):30398–409. doi:10.1109/access.2019.2895062
36. Wu JY, Huang WL, Xia-Hou WM, Zou WP, Gong LH. Imperceptible digital watermarking scheme combining 4-level discrete wavelet transform with singular value decomposition. *Multimedia Tools Appl* (2020) 79:22727–47. doi:10.1007/s11042-020-08987-3
37. Eastman Kodak Company. Kodak lossless true color image suite—Photo CD PCD0992. Available online: <http://r0k.us/graphics/kodak/index.html> (accessed on 26 April 2021).